J Mater Sci: Mater Electron (2015) 26:1625–1633
DOI 10.1007/s10854-014-2586-7

Arrays of $Zn_xCd_{1-x}Se/TiO_2$ nanotubes: fabrication by ion-exchange and photovoltaic applications

Zhen Li · Libo Yu · Yingbo Liu · Shuqing Sun

Received: 14 October 2014 / Accepted: 5 December 2014 / Published online: 11 December 2014

Abstract Free-standing TiO_2 nanotube (NT) array films were prepared by anodization approach as support materials for quantum dots sensitized solar cells (QDSSCs). The $Zn_xCd_{1-x}Se$ quantum dots (QDs) layers with tunable compositions have been deposited on the TiO_2 NT array film via a simple ion-exchange approach. The optical absorptions of the $Zn_xCd_{1-x}Se/TiO_2$ NT can be controllably tuned to cover almost the entire visible region by changing the atomic ratio of Zn to Cd. In the fabricated QDSSCs based on these $Zn_xCd_{1-x}Se/TiO_2$ NT array photoanodes, the photovoltaic performance gradually improved as the composition changes from Zn-rich to Cd-rich of $Zn_xCd_{1-x}Se$ QDs layers on TiO_2 NT arrays. In contrast with other $Zn_xCd_{1-x}Se/TiO_2$ NT solar cells, the $Zn_{0.13}Cd_{0.87}Se/TiO_2$ NT solar cell yielded a highest power conversion efficiency of 2.15 %, indicating the most effective band alignment is obtained with Cd-rich $Zn_xCd_{1-x}Se$ QDs layers. It can be anticipated that tunable energy band of QDs controlled by the ratio of atoms can contribute to higher efficiency QDSSCs.

1 Introduction

The development of one-dimensional nanostructure materials including nanorods, and nanotubes that can be used as substrate in photovoltaic system is quite a challenging subject [1, 2]. The vertically aligned one-dimensional architectures provide a direct pathway for rapid transport of photogenerated carriers to the collection electrodes [3]. In particular, TiO_2 nanotube (NT) arrays sheathed with semiconductor nanocrystals are emerging as novel photoelectrode for photoelectrochemical cells [4, 5]. Band gap engineering is an important strategy for custom tuning physical properties of semiconductors in photoelectronic devices. On comparison with bulk semiconductors, nanocrystals which are also known as quantum dots (QDs) provide a novel way for band gap modulation through their tunable sizes and shapes due to the quantum confinement effects [6].

Recently, much attention has been paid on QD sensitized solar cells (QDSSCs) based on one-dimensional TiO_2 NT arrays, sensitized by various QDs such as CdS [7], CdSe [8], and CdTe [9]. However, power conversion efficiencies of these QDSSCs are usually in a low level. The co-sensitization of different component QDs is a promising technique to improve the efficiency of QDSSCs. For instance, CdS/CdSe system showed higher solar cell efficiency than either of the single QDs [10–13]. Ternary alloyed QDs have also been employed as efficient sensitizers due to their advantage of tunable band gap by varying their relative composition [14–17]. Furthermore, gradient heterostructures can be formed in alloyed QDs to engineering band gap. For example, ZnO–$Zn_xCd_{1-x}Se$ core/shell nanowire arrays have band-gaps that from a stepwise energy alignment at the heterojunctions, where both the conduction and valence bands of the shell are either higher or lower in energy than those of core [18, 19]. The photogenerated electrons and holes would preferably transfer across the interface in opposite directions to form a charge separation state.

Electronic supplementary material The online version of this article (doi:10.1007/s10854-014-2586-7) contains supplementary material, which is available to authorized users.

Z. Li · L. Yu · Y. Liu · S. Sun (✉)
Department of Chemistry, Tianjin University, Tianjin 300072, People's Republic of China
e-mail: sunshuqing@tju.edu.cn

Herein, we design and report an ion-exchange route to prepare $Zn_xCd_{1-x}Se$ layers on a pre-anodic TiO_2 NT arrays with tunable composition ($0 \leq x \leq 1$) and band-gaps from 1.80 to 2.67 eV. The strategy for the synthesis of $Zn_xCd_{1-x}Se/TiO_2$ NT arrays is based on the difference between solubility product constant (K_{sp}) of ZnSe and CdSe [20]. The K_{sp} of ZnSe (3.6×10^{-26}) is larger than the K_{sp} of CdSe (6.31×10^{-36}), which implies that the pre-prepared $ZnSe/TiO_2$ NT arrays can be used as sacrificial templates to convert into $Zn_xCd_{1-x}Se/TiO_2$ NT arrays by cation exchange between Zn^{2+} and Cd^{2+}. Although alloyed QDs sensitized solar cells have been reported in previous research work [16, 18, 21], surprisingly, the QDSSCs based on $Zn_xCd_{1-x}Se/TiO_2$ NT photoanode synthesized by ion-exchange route has rarely referred. On the basis of the $Zn_xCd_{1-x}Se/TiO_2$ NT arrays, a photovoltaic device with a maximum power conversion efficiency of 2.15 % has been demonstrated. Based on the experimental results, a possible formation mechanism involving the band alignment has been proposed in this study.

2 Experiments

2.1 Chemicals

Titanium (Ti) foils (99.6 % purity), ammonium fluoride (NH_4F), ethylene glycol ($HOCH_2CH_2OH$), hydrogen peroxide (30 wt% H_2O_2), deionized water (H_2O, 18.2 ΩM cm resistivity), ethyl cellulose, terpinol ($C_{10}H_{18}O$), tetrabutyl titanate ($Ti(OC_4H_9)_4$), zinc acetate dihydrate ($Zn(AC)_2 \cdot H_2O$), cadmium nitrate tetrahydrate ($Cd(NO)_3 \cdot 4H_2O$), and selenium powder (Se) were employed as starting materials. Unless otherwise indicated, all these reagents used were of analytical purity and were used directly, without further purification.

2.2 Experimental details

2.2.1 *Fabrication of crystallized and free-standing TiO_2 NT films*

Titanium foils were cut into the required size and shape, following by being cleaned in acetone, ethanol and deionized water, respectively, then dried in air and processed for anodization. The free-standing TiO_2 NT films were prepared by a two-step potentiostatic anodization in a two-electrode electrochemical cell similar to previous report [22]. Ti foil is used as the anode and graphite sheet as the cathode. The Ti foil was first anodized in a electrolyte solution consisted of 150 mL ethylene glycol, 0.3 wt% NH_4F, and 3 vol% deionized water at 50 V using a laboratory DC power supply for 8 h. The first anodized products were rinsed with ethanol and slightly ultrasonicated in ethanol to remove debris adsorbed on the surface, and dried in ambient temperature. The as-prepared TiO_2 NT film on Ti foil was annealed at 450 °C for 1 h to ensure the complete crystallization. Following this annealing treatment, the annealed TiO_2 NT film on Ti foil was anodized again with applied voltage of 10 V for 6 h in the electrolyte which was used in the first anodization process. After being rinsed in ethanol, the re-anodized products were immersed into 10 wt% H_2O_2 aqueous solution for another 6 h to resolve the new formed amorphous TiO_2 layer beneath the crystallized as-prepared TiO_2 NT film. This post-treatment will lead to gradual detachment of the crystalline TiO_2 NT membrane from the Ti substrate.

2.2.2 *Fixation of TiO_2 NT film on FTO glass photoanode*

A paste used as adhesive was prepared by mixing 0.5 mL tetrabutyl titanate, 0.5 g ethyl cellulose, 15 mL terpinol, and 5 mL ethanol, followed by magnetic stirring at 60 °C until transparent. Fluorine-doped tin oxide (FTO) conductive glass (OPV-FTO22-7, Liaoning, China) with 2 cm × 1.5 cm in size was employed as substrate and cleaned by rinsing in an ultrasonic bath of acetone and isopropanol for 20 min in turn, then rinsing with a large amount of ethanol and finally blowing to dry with a drier. The edges of the FTO glass were covered with scotch tape as the frame. The paste which functioned as adhesive was flattened with a glass rod on the surface of FTO glass. The free-standing TiO_2 NT film was then transferred onto the paste followed by drying the film at ambient temperature. In order to completely eliminate the organic component in the paste, the TiO_2 NT film on FTO glass was sintered again at 450 °C for 30 min.

2.2.3 *Fabrication of $Zn_xCd_{1-x}Se/TiO_2$ NT photoanode by ion-exchange method*

A Se source solution (0.1 M $NaSeSO_3$) was prepared by refluxing Se powder and $NaSO_3$ at 96 °C for 12 h in advance. The successive ionic layer adsorption and reaction (SILAR) cycles process similar to previous report [23] was used to prepare $ZnSe/TiO_2$ NT arrays template which involved dipping the TiO_2 NT film in a 0.1 M $Zn(AC)_2$ aqueous solution for 5 min, rinsing it with ethanol, and then dipping it for another 5 min in a 0.1 M $NaSeSO_3$ aqueous solution, and rinsing it again with ethanol. The two-step dipping procedure is termed as one SILAR cycle. In this experiment, 15 SILAR cycles were repeated to ensure the enough amount of ZnSe can be incorporated onto the TiO_2 NT film.

The $Zn_xCd_{1-x}Se/TiO_2$ NT photoanodes were obtained by the immersion of the $ZnSe/TiO_2$ NT template into a

Cd^{2+} source solution (0.1 M $Cd(NO)_3$ aqueous solution) at 90 °C for different periods (4, 8 and 12 h). In this process, the cation of Cd^{2+} will gradually substitutes the Zn^{2+} in the ZnSe, forming $Zn_xCd_{1-x}Se$ with different atomic ratios of Cd to Zn. The variation of Zn and Cd in $Zn_xCd_{1-x}Se$ can be tuned by controlling the reaction time of the ZnSe/TiO_2 NT template with the Cd^{2+} ions.

For photovoltaic applications, the prepared $Zn_xCd_{1-x}Se$/TiO_2 NT photoanodes were assembled with Pt/FTO counter electrode which prepared by pyrolysis of hydrochloroplatinic acid in a fashion similar to sandwich. The space between the two electrodes was filled with polysulfide electrolyte as holes scavenger which was consisted of 0.5 M sodium sulfide, and 0.1 M sulfur aqueous solution.

2.3 Characterization

Field-emission scanning electron microscopy (SEM) and transmission electron microscopy (TEM) were carried out with a Hitachi S-4200 field emission SEM and a Tecnai G2 F20 TEM, respectively. The compositional analysis and elemental mapping of the as-prepared sample were performed with an energy-dispersive X-ray spectroscopy (EDX), an accessory of the SEM. The crystalline nature and structure of the TiO_2 NT films were characterized by X-ray diffraction (XRD, D/MAX-2400, Rigaku) using a Cu Kα source operated at 40 kV and 30 mA with scanning rate of 4° min. The optical absorption of the samples was recorded using a UV2501PC (SHIMADZU) spectrometer with an ISR-2200 integrating sphere attachment for diffuse reflection measurement.

The photocurrent–voltage (*J*–*V*) curves were measured under an illumination of a solar simulator (Pecell-L15, Japan) at one sun (AM1.5, 100 mW cm^{-2}), which calibrated by standard silicon solar cell (BS-520, Japan). The incident photon-to-current conversion efficiency (IPCE) was measured as a function of wavelength from 300 to 800 nm by employing a 150-W Xe lamp coupled with a computer-controlled monochromator. A mask with exposure area of 0.16 cm^2 was used to cover on the photoanodes when conducting photovoltaic measurement.

3 Results and discussion

Figure 1a shows the SEM image of the as-prepared TiO_2 NT arrays. It can be seen that the TiO_2 NT arrays are highly ordered distributed over the entire surface. The tubular structure with a nearly uniform wall thickness possesses an outer diameter approximate to 100 nm. The inset of Fig. 1a is the part cross-section view of the TiO_2 NT arrays, showing that the nanotubes regularly aligned together. The growth direction of the TiO_2 NT is also pointed as the arrow indicates, showing that the TiO_2 NTs were vertically grown. The evolution of the TiO_2 NT is an electrochemical etching process accompanying with two main reactions [24]:

$$Ti + 2H_2O \rightarrow TiO_2 + 4H^+ + 4e^- \quad (1)$$

$$TiO_2 + 4H^+ + 6F^- \rightarrow [TiF_6]^{2-} + 2H_2O \quad (2)$$

Initially, TiO_2 layer is formed on the surface of Ti foil under anodization as reaction (1) indicated, meantime, reaction (2) occurs, the F^- begin to etching the TiO_2 layer to form pits on the its surface, which is called 'pitting attack' process. As the anodization time prolongs, the pits would be gradually developed into tubular structure.

Figure 1b presents the back-side morphology of the free-standing TiO_2 NT film, displaying that the bulges of TiO_2 NT arrays are packed in approximately circle shape and possess sealed ends, and the integrity of the arrays preserves well. The whole free-standing TiO_2 NT film detached from Ti foil is presented in the inset of Fig. 1b, exhibiting a light brown color and translucence, which indicates its potential application as photoanode materials in sensitized solar cells. The TEM image of the free-standing TiO_2 NT arrays is shown in Fig. 1c. Obviously, the TiO_2 NTs aligned with each other and have hollow tubular structure, providing the space for adsorption of ZnSe QDs and channels for excited electrons to transport in sensitized solar cells. Figure 1d shows the TEM of a single TiO_2 NT in large magnification, from which the hollow tubular structure can be clearly identified. The inner and outer diameter of the nanotube can be estimated to be around 80 and 100 nm, respectively, which is almost consistent with the SEM result, and the wall thickness of the TiO_2 NT is around 20 nm. The selected area electron diffraction (SAED) pattern from the TEM of the free-standing TiO_2 NT is displayed in the inset of Fig. 1d. The appearance of diffraction rings indicates that the free-standing TiO_2 film obtained from two-step anodization process is in polycrystalline phase (Fig. 2).

The XRD data reveal that the TiO_2 NT film experienced a phase transformation between the first and second step anodization process. Figure 2*a* is the XRD patterns of the first anodized TiO_2 NT film (without annealing treatment) which scraped from the Ti substrate. None of diffraction peaks can be observed in this XRD pattern, indicating that the TiO_2 NT film formed in the first anodization process is in amorphous phase. However, strong diffraction peaks appeared for the free-standing TiO_2 NT film obtained from the second step anodization. This phase transformation can be ascribed to the annealing treatment of the first anodized Ti foil, which changes the amorphous TiO_2 NT to the crystalline TiO_2 NT. The crystallized TiO_2 is critical for the successful separation of TiO_2 NT film due to the

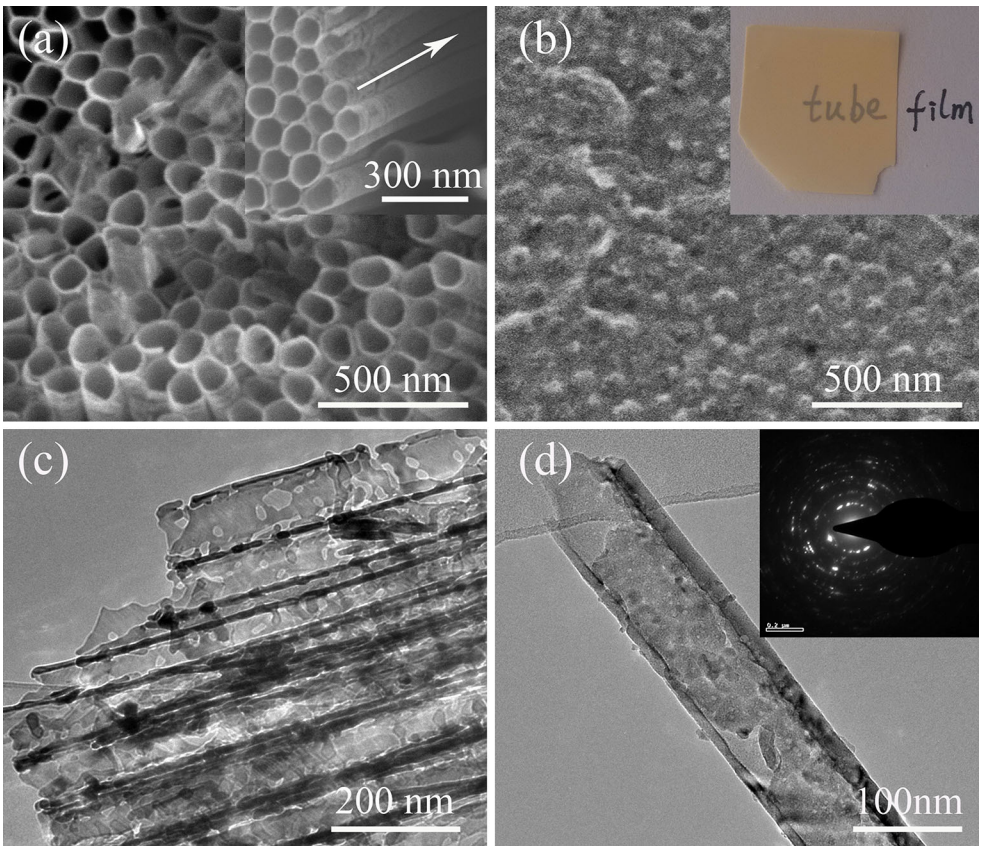

Fig. 1 **a** Top morphology of the separated TiO_2 NT film, *inset* is part of cross-section view, **b** back-side morphology of the TiO_2 NT film, *inset* is the digital photograph of the separated TiO_2 NT film, **c** TEM image of TiO_2 NTs, **d** TEM of single TiO_2 NT, and *inset* is its corresponding SAED pattern

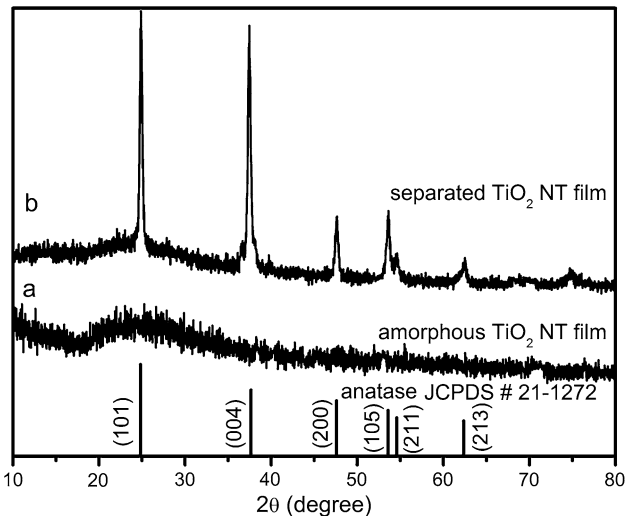

Fig. 2 XRD patterns of *a* TiO_2 NT film scraped from first anodized Ti foil without annealing treatment, *b* annealed TiO_2 NT film separated by being immersed in H_2O_2 solution

chemical stability of the crystallized TiO_2 to H_2O_2 aqueous solution [22]. A new amorphous TiO_2 layer would be formed between crystallized TiO_2 NT and Ti foil during secondary anodization process, and this amorphous layer TiO_2 can be resolved by 10 wt% H_2O_2 aqueous solution, leading to the separation of crystallized TiO_2 NT film from Ti substrate. For comparison, the standard XRD pattern of anatase TiO_2 (JCPDS # 21-1272) is supplied. The diffraction peaks corresponding to (101), (004), (200), (105), (211) and (213) planes confirm that the free-standing TiO_2 NT film belong to the anatase TiO_2.

Figure 3a shows the SEM image of the $Zn_xCd_{1-x}Se/TiO_2$ NT arrays which is obtained by ion-exchange of $ZnSe/TiO_2$ NT photoanode in Cd^{2+} solution for 8 h. Obviously, the $Zn_xCd_{1-x}Se/TiO_2$ NT arrays have a reduced inner diameter and rougher surface than that of the bare TiO_2 NT arrays, indicating the successful adsorption of sensitizers into the TiO_2 NT arrays. The structures of the $Zn_xCd_{1-x}Se/TiO_2$ NT arrays are further demonstrated by their TEM images. Figure 3b exhibits a typical TEM image of the $Zn_xCd_{1-x}Se/TiO_2$ NT arrays. Evidently, a large amount of nanoparticles are distributed across the nanotubes. Figure 3c provides the TEM image of single $Zn_xCd_{1-x}Se/TiO_2$ NT in higher magnification, clearly showing the tubular structure as the scaffold to support nanoparticles. As illustrated in Fig. 3d, the EDX elemental mapping

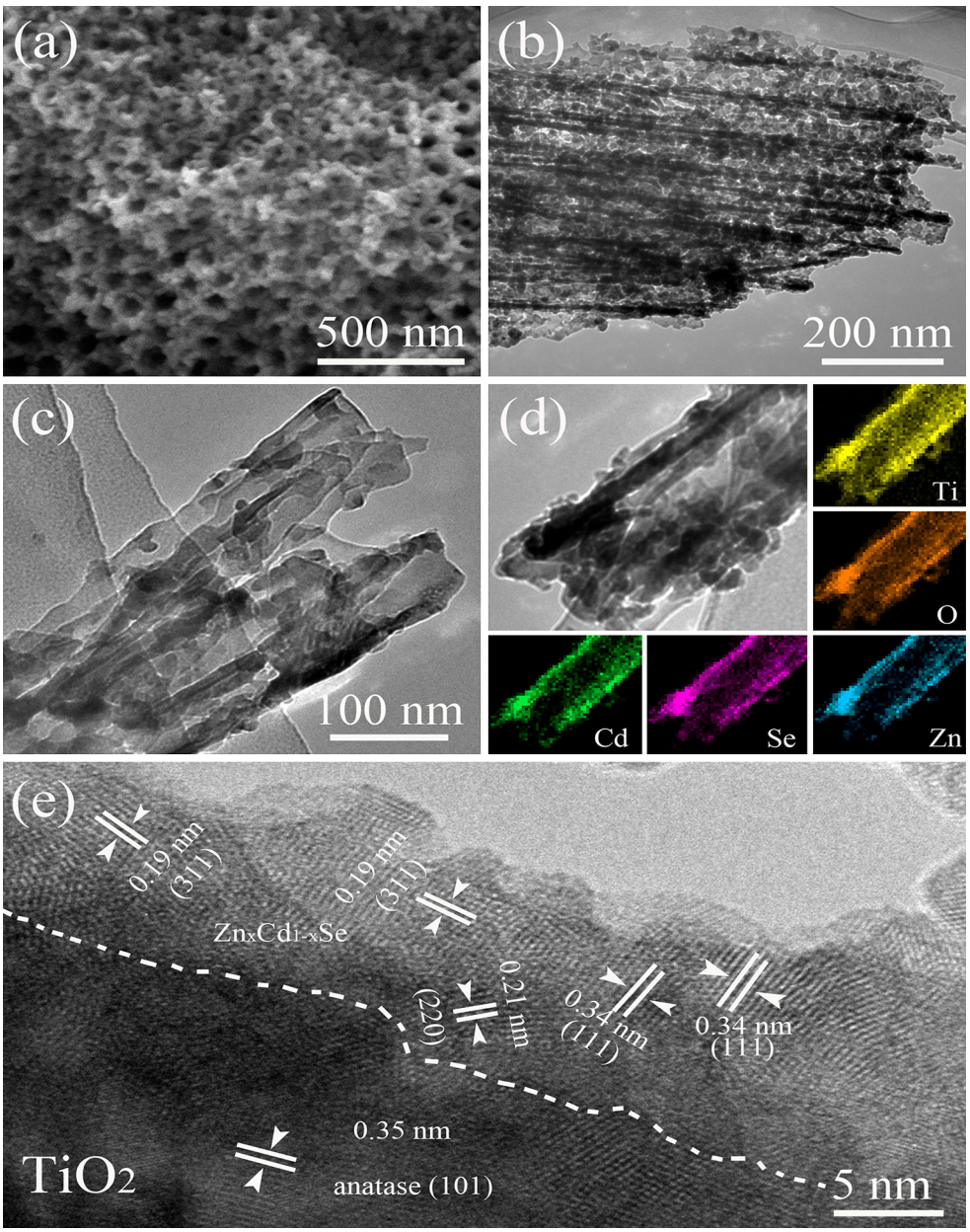

Fig. 3 **a** SEM of $Zn_xCd_{1-x}Se/TiO_2$ NT film, **b** TEM of $Zn_xCd_{1-x}Se/TiO_2$ NT film, **c** large magnification TEM of $Zn_xCd_{1-x}Se/TiO_2$ NT, **d** elemental mapping of the $Zn_xCd_{1-x}Se/TiO_2$ NT, **e** HRTEM of $Zn_xCd_{1-x}Se/TiO_2$ NT. All samples were obtained from ion-exchange of $ZnSe/TiO_2$ NT photoanode in Cd^{2+} solution for 8 h

confirms that the presence and distribution of the Zn, Cd and Se elements which are based on TiO_2 NT. Figure 3d is the HRTEM image of the $Zn_xCd_{1-x}Se/TiO_2$ NT prepared by ion-exchange of $ZnSe/TiO_2$ NT photoanode in Cd^{2+} solution for 8 h. The observed lattice spacing of 0.35 nm corresponds to the (101) plane of anatase TiO_2, confirming that the supporter of the sensitizers is TiO_2. Along the TiO_2 crystalline edge, fine crystallites could be discerned. The crystallites close to TiO_2 have lattice fringe of 0.34, 0.21, and 0.19 nm, which can be ascribed to the (111), (220), and (311) planes of $Zn_xCd_{1-x}Se$. These results of SEM, TEM, and EDX elemental mapping characterization have confirmed that the successful formation of $Zn_xCd_{1-x}Se/TiO_2$ NT arrays can be obtained from the ion-exchange strategy of $ZnSe/TiO_2$ NT in Cd^{2+} solution.

In order to estimate the composition of $Zn_xCd_{1-x}Se$, EDX spectra and data were used to approximately calculate the x value of $Zn_xCd_{1-x}Se$. The EDX spectra of the $Zn_xCd_{1-x}Se/TiO_2$ NT and their corresponding quantitative data are shown in the supplementary material (Fig. S1). The $Zn_xCd_{1-x}Se/TiO_2$ NT obtained from ion-exchange process in various periods, with different compositions, are

Table 1 Composition of $Zn_xCd_{1-x}Se$ synthesized in the different ion-exchange periods

Ion-exchange periods	Zn/(Zn + Cd) (%)	Composition of $Zn_xCd_{1-x}Se$
0	100	ZnSe
4	64	$Zn_{0.64}Cd_{0.36}Se$
8	27	$Zn_{0.27}Cd_{0.73}Se$
12	13	$Zn_{0.13}Cd_{0.87}Se$

listed in Table 1. With regard to the EDX spectra in Fig. S1, the atomic ratio of Zn to Se is calculated to be around 1:1.19 for the $ZnSe/TiO_2$ NT (Fig. S1a). The deviation from a stoichiometric ratio of ZnSe is probably caused by the oxidation of Se^{2-} on the surface of the TiO_2 NT into amorphous Se, in the air [19]. After ion-exchange process of $ZnSe/TiO_2$ NT in the Cd cations solution for different periods, the EDX spectra (supplementary materials, Fig. S1b-d) indicates that the Cd^{2+} ions have replaced the Zn^{2+} to form $Zn_xCd_{1-x}Se$ on TiO_2 NT. The estimated results (Table 1) of the $Zn_xCd_{1-x}Se$ prepared in different time are presented as ZnSe, $Zn_{0.64}Cd_{0.36}Se$, $Zn_{0.27}Cd_{0.73}Se$, and $Zn_{0.13}Cd_{0.87}Se$, corresponding to ion-exchange time for 0, 4, 8, and 12 h, respectively.

The $Zn_xCd_{1-x}Se/TiO_2$ NT was prepared by ion-exchange process by immersing $ZnSe/TiO_2$ NT in Cd^{2+} solution. This ion-exchange reaction occurred on the surface between ZnSe layers and Cd^{2+} solution as the following reaction (3) indicated:

$$ZnSe + Cd^{2+} \rightarrow CdSe + Zn^{2+} \quad (3)$$

Therefore, it is reasonable to speculate that a composition gradient $Zn_xCd_{1-x}Se$ with three different phases would probably be formed due to the diffusion of Cd^{2+} from surface of ZnSe layers to the deep layer of ZnSe, which is illustrated in Fig. 4. Initially, once the $ZnSe/TiO_2$ NT is immersed into the Cd^{2+} solution, the Cd^{2+} would substitute some of Zn^{2+} for form $Zn_xCd_{1-x}Se$ fast. However, the quickly formed $Zn_xCd_{1-x}Se$ layer upper the ZnSe layers could prevent the Cd^{2+} from further infusing into the deep layers of ZnSe to replace Zn^{2+}, and in contrast the upper layer would be rich of Cd, leading to form a gradient composition with CdSe, $Zn_xCd_{1-x}Se$, and ZnSe as upper, middle, and deep layers (indicated in A and B selected zone in Fig. 4), respectively. The similar gradient composition of $Zn_xCd_{1-x}Se$ has also been observed in previous report by Yang et al. [19].

The current density–voltage (*J–V*) performance curves of the solar cells, assembled with $Zn_xCd_{1-x}Se/TiO_2$ NT photoanodes, Pt/FTO counter electrodes and electrolyte based on mixture of 0.5 M sodium sulfide and 0.1 M sulfur aqueous solution, are presented in Fig. 5. The photovoltaic

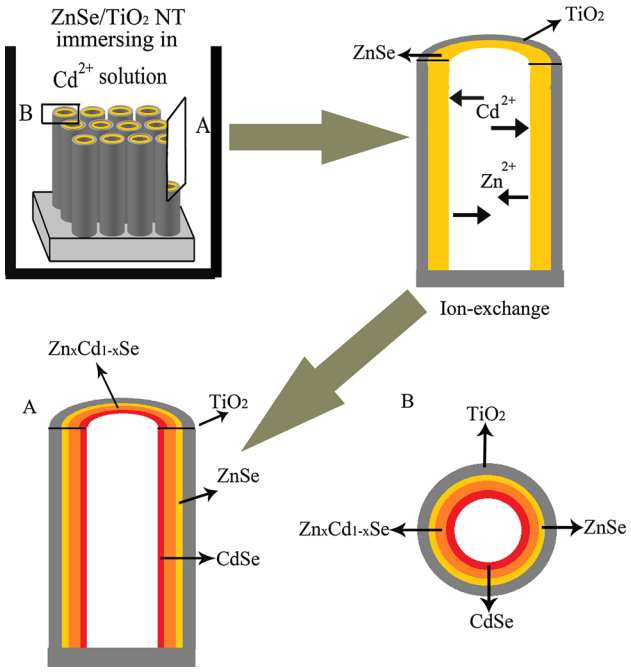

Fig. 4 Possible mechanism for the formation of $Zn_xCd_{1-x}Se/TiO_2$ NT with a composition gradient

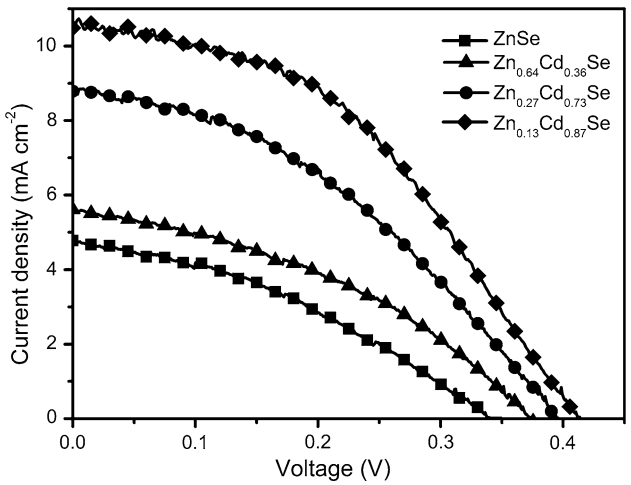

Fig. 5 Current density–voltage (*J–V*) characteristics of the solar cells based on the photoanodes of $Zn_xCd_{1-x}Se/TiO_2$ NT array film

parameters of the $Zn_xCd_{1-x}TiO_2$ NT solar cells including short circuit current density (J_{sc}), open circuit voltage (V_{oc}), fill factor (FF), and power conversion efficiency (PCE) are also summarized in Table 2. The solar cell based on $ZnSe/TiO_2$ NT photoanode exhibits a J_{sc} of 4.78 mA cm^{-2}, a V_{oc} of 0.34 V, and a FF of 0.36, producing a PCE of 0.59 %. With increasing Cd content in the $Zn_xCd_{1-x}Se$ QDs, the photovoltaic parameters are also gradually enhanced. The solar cell based on $Zn_{0.64}Cd_{0.36}Se/TiO_2$ NT photoanode gives a J_{sc} of 5.61 mA cm^{-2}, a V_{oc} of 0.37 V, and a FF of

Table 2 Photovoltaic parameters obtained from the *J–V* curves using $Zn_xCd_{1-x}Se/TiO_2$ NT array film as photoanodes

Composition	J_{sc} (mA cm^{-2})	V_{oc} (V)	FF	PCE (%)
ZnSe	4.78	0.34	0.36	0.59
$Zn_{0.64}Cd_{0.36}Se$	5.61	0.37	0.38	0.79
$Zn_{0.27}Cd_{0.73}Se$	8.79	0.40	0.49	1.72
$Zn_{0.13}Cd_{0.87}Se$	10.49	0.41	0.50	2.15

0.38, yielding a PCE of 0.79 %. The $Zn_{0.27}Cd_{0.73}Se/TiO_2$ NT solar cell shows a drastically improved J_{sc} of 8.79 mA cm^{-2}, a V_{oc} of 0.4 V, and a FF of 0.49, leading to a PCE of 1.72 %. Compared with the other sample solar cells, the solar cells based on $Zn_{0.13}Cd_{0.87}Se/TiO_2$ NT photoanode produces a further enhanced J_{sc} of 10.49 mA cm^{-2}, V_{oc} of 0.41 V, and FF of 0.50, yielding the PCE of 2.15 %. The significant improvement of photovoltaic performance for the solar cells based on various of Zn_xCd_{1-x}/TiO_2 NT photoanode is mainly attributed to a broader light absorption, a more effective generation of photoexcited electrons, and a more efficient electron injection efficiency. The specific reasons will be further discussed later.

Compared with the $ZnSe/TiO_2$ NT solar cell, the solar cells based on $Zn_xCd_{1-x}Se/TiO_2$ NT photoanodes with different composition could effectively improve the photoelectric conversion efficiency due to a broader absorption of visible light as the increase of Cd content in $Zn_xCd_{1-x}Se$. The UV–Vis absorption spectra of the bare TiO_2 NT, $ZnSe/TiO_2$ NT, $Zn_{0.64}Cd_{0.36}Se/TiO_2$ NT, $Zn_{0.27}Cd_{0.73}Se/TiO_2$ NT, and $Zn_{0.13}Cd_{0.87}Se/TiO_2$ NT photoanodes were characterized and the results are shown in Fig. 6. It could be observed that the bare TiO_2 NT exhibits an absorption onset at around 380 nm, which corresponds to the band gap of anatase TiO_2 (3.26 eV) [25]. The absorption edge of $ZnSe/TiO_2$ NT at around 450 nm, corresponding to the band gap of 2.75 eV, which is higher than the band gap of ZnSe in bulk (2.67 eV) [15], suggesting that the ZnSe particles deposited on TiO_2 NT are within the scale of QDs. Further expanded absorption edge in the visible light region is demonstrated upon the formation of $Zn_xCd_{1-x}Se$ alloyed QDs. As the increase of Cd relative atomic ratio in the $Zn_xCd_{1-x}Se$ alloyed QDs, the absorption edge of the photoanodes is gradually red-shifted to around 530 ($Zn_{0.64}Cd_{0.36}Se/TiO_2$ NT), 600 ($Zn_{0.27}Cd_{0.73}Se/TiO_2$ NT), and 690 nm ($Zn_{0.13}Cd_{0.87}Se/TiO_2$ NT), corresponding the band gap of 2.34, 2.07, and 1.80 eV, respectively. This expanded absorption range in visible light region shows that the decrease of the optical band gap stems from the stoichiometry variation in the composition of the $Zn_xCd_{1-x}Se$ alloy semiconductors. Thus, it can be concluded that the Cd-rich composition of $Zn_xCd_{1-x}Se$ semiconductors amplify the photon absorption at the longer wavelength,

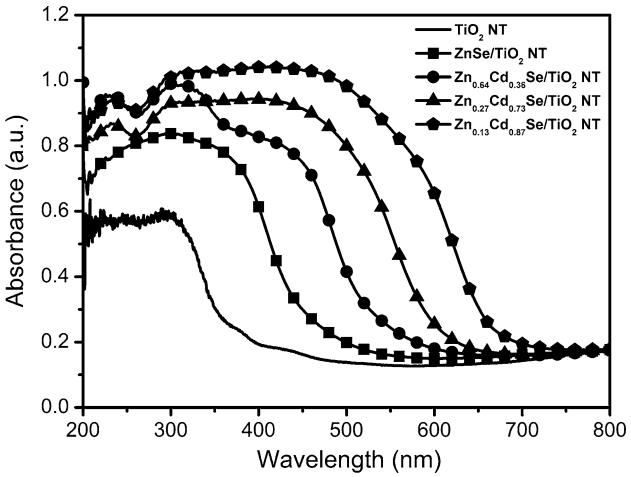

Fig. 6 UV–Visible absorption spectra obtained with bare TiO_2 NT and various $Zn_xCd_{1-x}Se/TiO_2$ NT photoanodes

which means more photons would be involved in the generation of photoexcited electrons, leading to an improved light harvesting efficiency.

The maximum J_{sc} of 10.49 mA cm^{-2} obtained from $Zn_{0.13}Cd_{0.87}Se/TiO_2$ NT solar cell can be attributed to the expanded absorption range in visible light region. Here, J_{sc} is determined by the following equation:

$$J_{sc} = q\eta_{lh}\eta_{ing}\eta_{cc}I_o \quad (4)$$

where q is the elementary charge, I_o is the incident photon flux of light (6.6×10^{16} cm^{-2}S^{-1}), η_{lh} is the light harvesting efficiency, η_{ing} is the charge injection efficiency, and η_{cc} is the charge collection efficiency [26]. As discussed earlier, the increase of Cd content in $Zn_xCd_{1-x}Se$ alloy semiconductors significantly enlarge the visible light absorption range. Moreover, the light absorption was expanded to the nearly entire visible light region with $Zn_{0.13}Cd_{0.87}Se$, which drastically improve the η_{lh} of $Zn_{0.13}Cd_{0.87}Se/TiO_2$ NT photoanode, thus resulting the increment of J_{sc}.

The IPCE spectra was monitored to compare the photoresponse of $Zn_xCd_{1-x}Se/TiO_2$ NT photoanodes, which is presented in Fig. 7. Comparison of these IPCE spectra yields two interesting observations. The first observation is the ability to tune the photoresponse of the photoanodes by controlling the Cd content in $Zn_xCd_{1-x}Se$. Similarities between the IPCE spectra and absorption spectra confirm the excitation of the $Zn_xCd_{1-x}Se$ as the primary event responsible for photocurrent generation. The onset in photocurrent gradually shift to the red region with increasing Cd content in $Zn_xCd_{1-x}Se$ is in agreement with the expanded absorption at longer wavelengths, which further confirmed that the light harvesting efficiency could be enhanced by forming Cd-rich $Zn_xCd_{1-x}Se$ alloy QDs on TiO_2 NT. The second observation is that the maximum

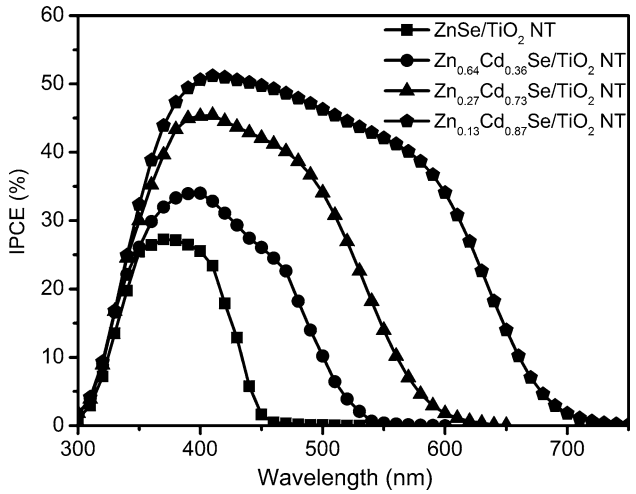

Fig. 7 The incident photo-to-current conversion efficiency (IPCE) spectra of various solar cells based on different $Zn_xCd_{1-x}Se/TiO_2$ NT photoanodes

IPCE value for various $Zn_xCd_{1-x}Se/TiO_2$ NT photoanodes is on the rise with increasing Cd content. This incremental trend of IPCE may be attributed to the gradient composition of $Zn_xCd_{1-x}Se$, forming a stepwise structure of conduction band edge alignment in order of $ZnSe < Zn_xCd_{1-x}Se < CdSe$, which favours the collection of photoexcited electrons to the conduction band of TiO_2 NT, leading to improvement of the charge collection efficiency. As a result, the maximum IPCE of 52 % with photocurrent onset around 690 nm, which obtained by the $Zn_{0.13}Cd_{0.87}Se/TiO_2$ NT photoanode, highlights the contribution to the significant increase of J_{sc} by forming Cd-rich $Zn_xCd_{1-x}Se$ alloy semiconductors.

It is well-known that the band alignment of semiconductors in the photosensitizing architecture has an important effect on the electron injection from photoexcited QDs to the conduction band of TiO_2, which influence the open circuit voltage (V_{oc}) of QDSSCs. The V_{oc} can be determined by the following equation [27]:

$$V_{oc} = \frac{E_{Fn} - E_{redox}}{e} = \frac{k_B T}{e} \ln(n/n_0) \quad (5)$$

where E_{fn} is the quasi-Fermi level of the electrons in semiconductor photoanode under illumination; E_{redox} is the potential of redox electrolyte; e is the positive elementary charge; k_BT is the thermal energy; n is the electron concentration in conduction band of the semiconductor photoanode under illumination; n_0 is the electron concentration in the dark condition. When the collection and injection efficiency of electrons are increased, more electrons would be accumulated in the conduction band of TiO_2, which results in an increment of n, while the E_{redox} remains unchangeable. This accumulation of electrons in conduction band of TiO_2 is related with the band positions of

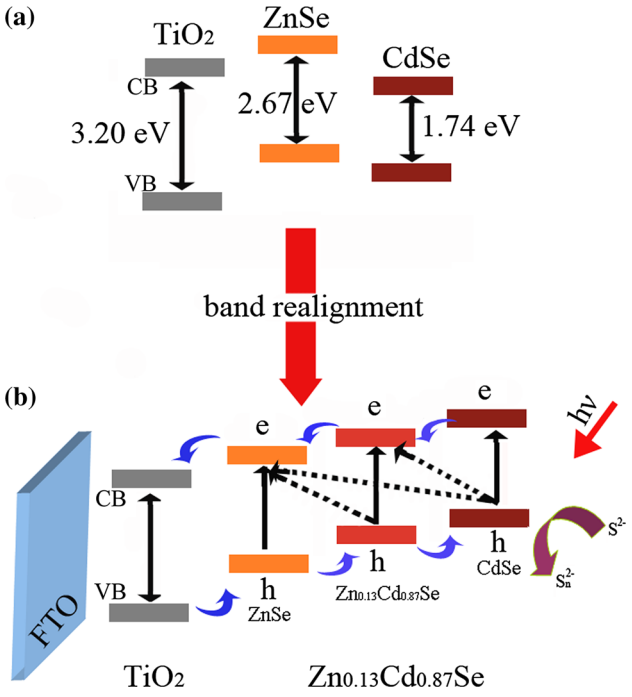

Fig. 8 **a** Band positions of TiO_2, ZnSe, and CdSe in bulk, **b** band realignment model in $Zn_{0.13}Cd_{0.87}Se$ QDs sensitized TiO_2 NT photoelectrode

semiconductor sensitizers. Figure 8a exhibits the band positions of TiO_2, ZnSe, and CdSe in bulk, showing that ZnSe has a higher conduction band edge in comparison with that of TiO_2 NT, which is beneficial to the injection of photoexcited electron from ZnSe. On the contrary, the CdSe has a lower conduction band edge than that of TiO_2 NT, leading to a less efficient electron injection from CdSe. However, when TiO_2, ZnSe, and CdSe are brought in contact as cascade architecture, the energy levels difference between ZnSe and CdSe would result in the electrons flow from ZnSe to CdSe, which is known as Fermi level alignment [11]. This redistribution of the electrons between ZnSe and CdSe can trigger a downward and upward shift of the band edges for ZnSe and CdSe respectively, leading to a large driving force for the injection of photoexcited electrons to the conduction band of TiO_2 NT. Therefore, a band realignment model, as illustrated in Fig. 8b, is proposed for the $Zn_{0.13}Cd_{0.87}Se/TiO_2$ NT photoanode. It is simply supposed that the $Zn_{0.13}Cd_{0.87}Se/TiO_2$ NT photoanode possesses a gradient structure with ZnSe as inner layer (Zn-rich layer), $Zn_{0.13}Cd_{0.87}Se$ as intermediate layer, and CdSe as out layer (Cd-rich layer). Based on this gradient structure, a realignment of the band positions among Zn-rich inner layer, $Zn_{0.13}Cd_{0.87}Se$ intermediate layer, and Cd-rich outer layer occurs to form a step-wise band position structure, which is favorable to the collection and injection of photoexcited electrons to the conduction band of TiO_2 NT. It can be concluded that such a gradient

structure induces a synergistic effect, which increases the electron collection efficiency and driving force for accumulation of electrons in conduction band of TiO_2, resulting in an enhancement V_{oc} of solar cells.

4 Conclusion

In summary, the Zn_xCd_{1-x}/TiO_2 NT photoanode have been constructed through a facile ion-exchange process after the formation of ZnSe QDs on translucent TiO_2 NT array film for QDSSCs. The light absorption property of ternary Zn_xCd_{1-x} QDs layers can be tuned by changing the atomic ratio of Zn to Cd in alloyed Zn_xCd_{1-x} QDs. The power conversion efficiency of Zn_xCd_{1-x}/TiO_2 NT solar cells gradually enhanced as the increase of Cd content in Zn_xCd_{1-x} alloyed QDs. The gradient structure of $Zn_xCd_{1-x}Se$ layers composed of ZnSe (Zn-rich layer), Zn_xCd_{1-x} intermediate layer, and CdSe (Cd-rich layer) is proposed due to the diffusion of Cd cations. The band positions alignment of ternary sensitizers caused by the gradient structure contribute to the enhancement of photovoltaic performance for QDSSC based on $Zn_{0.13}Cd_{0.87}Se/TiO_2$ NT photoanode, yielding a maximum power conversion efficiency up to 2.15 %. Further investigation into the tunable energy band alloyed QDs with a range of atoms and ratios could be expected to improve the performance of QDSSCs. The flexibility of tailoring various materials via the simple ion-exchange approach makes it a very promising synthetic method for preparation of TiO_2 nanotube-based heterostructures with custom-designed properties for different applications.

Acknowledgments The authors gratefully acknowledge the support for this work from the Key Project of Tianjin Sci-Tech Support Program (No. 08ZCKFH01400).

References

1. K. Shankar, J.I. Basham, N.K. Allam, O.K. Varghese, G.K. Mor, X. Feng, M. Paulose, J.A. Seabold, K.-S. Choi, C.A. Grimes, J. Phys. Chem. C **113**, 6327 (2009)
2. K.S. Leschkies, R. Divakar, J. Basu, E. Enache-Pommer, J.E. Boercker, C.B. Carter, U.R. Kortshagen, D.J. Norris, E.S. Aydil, Nano Lett. **7**, 1793 (2007)
3. D.R. Baker, P.V. Kamat, Adv. Funct. Mater. **19**, 805 (2009)
4. W.-T. Sun, Y. Yu, H.-Y. Pan, X.-F. Gao, Q. Chen, L.-M. Peng, J. Am. Chem. Soc. **130**, 1124 (2008)
5. T. Toyoda, Q. Shen, J. Phys. Chem. Lett. **3**, 1885 (2012)
6. S. Rühle, M. Shalom, A. Zaban, ChemPhysChem **11**, 2290 (2010)
7. X. Ma, Y. Shen, Q. Wu, T. Shen, M. Cao, F. Gu, L. Wang, J. Inorg. Organomet. Polym. **23**, 798 (2013)
8. B. Mukherjee, Y.R. Smith, V. Subramanian, J. Phys. Chem. C **116**, 15175 (2012)
9. X.F. Gao, H.B. Li, W.T. Sun, Q. Chen, F.Q. Tang, L.M. Peng, J. Phys. Chem. C **113**, 7531 (2009)
10. J. Luo, L. Ma, T. He, C.F. Ng, S. Wang, H. Sun, H.J. Fan, J. Phys. Chem. C **116**, 11956 (2012)
11. Y.-L. Lee, Y.-S. Lo, Adv. Funct. Mater. **19**, 604 (2009)
12. B.-M. Kim, M.-K. Son, S.-K. Kim, N.-Y. Hong, S. Park, M.-S. Jeong, H. Seo, K. Prabakar, H.-J. Kim, Electrochim. Acta **117**, 92 (2014)
13. Z. Li, L. Yu, Y. Liu, S. Sun, J. Mater. Sci. **49**, 6392 (2014)
14. X. Song, M. Wang, J. Deng, Z. Yang, C. Ran, X. Zhang, X. Yao, ACS Appl. Mater. Interfaces **5**, 5139 (2013)
15. Y. Myung, J.H. Kang, J.W. Choi, D.M. Jang, J. Park, J. Mater. Chem. **22**, 2157 (2012)
16. T. Shu, Z. Zhou, H. Wang, G. Liu, P. Xiang, Y. Rong, H. Han, Y. Zhao, J. Mater. Chem. **22**, 10525 (2012)
17. A. Ranjitha, N. Muthukumarasamy, M. Thambidurai, D. Velauthapillai, R. Balasundaraprabhu, S. Agilan, J. Mater. Sci. Mater. Electron. **24**, 3014 (2013)
18. J. Xu, X. Yang, H. Wang, X. Chen, C. Luan, Z. Xu, Z. Lu, V.A. Roy, W. Zhang, C.-S. Lee, Nano Lett. **11**, 4138 (2011)
19. L. Yang, R. Zhou, J. Lan, Q. Zhang, G. Cao, J. Zhu, J. Mater. Chem. A **2**, 3669 (2014)
20. X. Wang, Q. Peng, Y. Li, Acc. Chem. Res. **40**, 635 (2007)
21. Q. Kang, Q. Cai, S.Z. Yao, C.A. Grimes, J. Ye, J. Phys. Chem. C **116**, 16885 (2012)
22. Q. Chen, D. Xu, J. Phys. Chem. C **113**, 6310 (2009)
23. H. Lee, M. Wang, P. Chen, D.R. Gamelin, S.M. Zakeeruddin, M. Grätzel, M.K. Nazeeruddin, Nano Lett. **9**, 4221 (2009)
24. S. Huang, W. Peng, C. Ning, Q. Hu, H. Dong, J. Phys. Chem. C **116**, 22359 (2012)
25. X. Chen, S.S. Mao, Chem. Rev. **107**, 2891 (2007)
26. J.-Y. Hwang, S.-A. Lee, Y.H. Lee, S.-I. Seok, ACS Appl. Mater. Interfaces **2**, 1343 (2010)
27. L. Yu, Z. Li, Y. Liu, F. Cheng, S. Sun, J. Power Sources **270**, 42 (2014)